

Comparison of Observed Galaxy Properties with Semianalytic Model Predictions using Machine Learning

MELANIE SIMET,^{1,2} NIMA CHARTAB SOLTANI,¹ YU LU,³ AND BAHRAM MOBASHER¹

¹*University of California Riverside, 900 University Ave, Riverside, CA 92521, USA*

²*Jet Propulsion Laboratory, California Institute of Technology, Pasadena, CA 91109, USA*

³*The Observatories, The Carnegie Institution for Science, 813 Santa Barbara Street, Pasadena, CA 91101, USA*

ABSTRACT

With large-scale galaxy surveys, we can observe hundreds of thousands of galaxies or more, up to billions with upcoming experiments such as WFIRST, Euclid and LSST. While such surveys cannot obtain spectra for all observed galaxies, we have access to the galaxy magnitudes in color filters. This data set behaves like a high-dimensional nonlinear surface, making it an excellent target for machine learning methods. In this work, we use a lightcone of semianalytic galaxies tuned to match CANDELS observations from Lu et al. (2014) to train a set of neural networks on a set of galaxy properties (stellar mass, metallicity, and average star formation rate) using the truth values from the semianalytic catalogs. We also demonstrate the effect of adding simulated observational noise to the simulated magnitudes, and then use neural networks trained on the noisy data to predict stellar masses, metallicities, and average star formation rates on real CANDELS galaxies, comparing our results to the physical parameters obtained from SED fitting. On semianalytic galaxies alone, we are nearly competitive with template-fitting methods. For the observed CANDELS data, our results are not as accurate, with indications that this inaccuracy is due to a combination of different assumptions in template-fitting and differences between the semianalytic models and the observed galaxies, particularly in the noise properties. Our results show that stellar mass, metallicity, and star formation rate can in principle be measured with neural networks at a competitive degree of accuracy and precision relative to physically motivated template-fitting methods if an appropriate training set can be obtained.

Keywords: galaxies: statistics, galaxies: fundamental parameters, methods: numerical

1. INTRODUCTION

Over the last decade, a number of wide-area spectroscopic surveys have been performed, including WiggleZ (Drinkwater et al. 2010), BOSS (Dawson et al. 2013), GAMA (Driver et al. 2012) and zCOSMOS (Lilly et al. 2007). These were used to measure spectral line diagnostics of physical conditions in galaxies to study the evolution of galaxies with look-back time. The results from these studies were often limited by Poisson noise due to the small number of galaxies when divided in terms of their redshifts or in physical parameter bins. In recent years the scale of such surveys have increased by many orders of magnitude in terms of both depth and area coverage. The on-going Dark Energy Survey (DES; Drlica-Wagner et al. 2018) and future Large Syn-

optic Survey Telescope (LSST; LSST Science Collaboration et al. 2009) will generate billions of galaxies with multi-waveband photometric data. These will soon join by space-based surveys like Euclid (Laureijs et al. 2011) and WFIRST (Spergel et al. 2015). Given their size, it is impossible to perform spectroscopic observations of individual galaxies. Therefore, techniques should be developed to measure the physical parameters associated with galaxies in these surveys, needed to study the programs they have been designed for.

The physical parameters for galaxies (redshift, stellar mass, star formation rate, extinction) are conventionally estimated by fitting their observed Spectral Energy Distributions (SEDs) to template SEDs that correspond to the type and class of galaxies in the observed sample. By shifting the model SEDs in redshift space, they are fitted to the observed SED. The template that provides the best fit to observations is then chosen, with its associated physical parameters assigned to the galaxy in question (Bolzonella et al. 2000; Brammer et al. 2008;

?). A serious problem in using template-fitting method is that the results depend on the type of the galaxies used in template models. For example, if the galaxy in question is not represented in the model templates, there will be serious uncertainties in the estimated parameters for that galaxy. Furthermore, apart from redshifts, for which a true estimate could be made (in the form of spectroscopic redshift) and used to measure its uncertainty, measuring a true value for other physical parameters is difficult and the results often do not directly correspond to the predicted value. Moreover, they suffer from photometric uncertainties, absence of a full photometric coverage and degeneracies between different parameters (Hildebrandt et al. 2010; Abdalla et al. 2011; Sánchez et al. 2014).

Recently, Machine Learning (ML) techniques have emerged as independent alternatives for measuring the physical parameters of galaxies (Sadeh et al. 2016; Ball et al. 2008; Hogan et al. 2015; Masters et al. 2015). Using a training sample with known physical parameters, they generate statistical models to predict the distribution of those parameters in a target data set. The ML techniques are only applicable within the limits of the training data. Any extrapolation of them to a different redshift or mass regime would lead to errors in the final estimate. However, a distinct advantage of ML is that one could incorporate extra information (i.e. morphology, galaxy light profile) within the algorithm. The ML techniques are divided into two categories: supervised and unsupervised. In supervised ML, the input attributes (magnitudes and colors) are provided along with the output (redshift) and directly used for training in the learning process (Lima et al. 2008; Freeman et al. 2009; Gerdes et al. 2010). Here, the learning process is supervised by the input parameters. The unsupervised techniques do not use the desired output values (e.g. spectroscopic redshifts) during the training with only the input attributes used. Due to its limitations, this is not frequently used.

The use of ML methods has so far been limited mainly to measuring photometric redshifts of galaxies. This is because the ML algorithms can be more easily trained using the spectroscopic redshifts whereas for other parameters such true and unambiguous estimates are hard to obtain. Detailed comparisons have been performed between different methods and algorithms measuring photometric redshifts (Carrasco Kind & Brunner 2013; Dahlen et al. 2013) and masses (Mobasher et al. 2015) of galaxies. However, except in a few cases where ML techniques are used (MCC and neural net) these were mostly based on different variants of template fitting using observed or model SEDs. In particular, very few

studies have performed a comparison of different ML techniques. A recent study has used Bayesian combination of photometric redshift Probability Density Functions (PDFs) using different ML methods to improve estimates of photometric redshifts (Carrasco Kind & Brunner 2014). However, no such study has been performed for other physical parameters of galaxies.

In this paper we use different ML techniques to measure the stellar mass and star formation rates of galaxies with available photometric data and photometric redshifts using a training set of semianalytic galaxies from (Lu et al. 2014). The test sample in this study is from the Hubble Space Telescope (HST) Cosmic Assembly Near-infrared Deep Legacy Survey (CANDELS) GOODS-South field. This has imaging data in optical (ACS) and near-infrared (WFC3) wavelengths as well as Spitzer Space Telescope mid-infrared (IRAC) bands. We describe the CANDELS data and semianalytic galaxies in section 2, give an overview of the neural network ML algorithm we use in section 3, test our neural networks with a semianalytic test set in section 4, and finally apply our networks to CANDELS data in section 5, with summary and conclusions in section 6. Throughout the paper, we assume the cosmology of the simulation used to generate the mock catalog and semianalytic galaxies: $\Omega_M = 0.27$, $\Omega_\Lambda = 0.73$, $\Omega_b = 0.044$, $h = 0.7$, $n = 0.95$, and $\sigma_8 = 0.82$.

2. DATA

2.1. CANDELS galaxies

The Cosmic Assembly Near-IR Deep Extragalactic Legacy Survey (CANDELS; Grogin et al. 2011; Koekoemoer et al. 2011) is a ~ 800 arcmin² survey performed using the Wide Field Camera 3 (WFC3) and Advanced Camera for Surveys (ACS) on the Hubble Space Telescope. The survey consists of five fields (GOODS-S, GOODS-N, COSMOS, EGS, and UDS). Multi-waveband photometric imaging observations were performed spanning the wavelength range from UV to mid-infrared. In two of these fields (GOODS-S and GOODS-N) deeper photometric observations over smaller areas were performed.

In this study, we use data from the GOODS-S deep field (Guo et al. 2013) covering an area of 170 arcmin². The combination of CANDELS pointings with supplementary data sets (Giavalisco et al. 2004; Riess et al. 2007; Bouwens et al. 2010; Windhorst et al. 2011) results in a multi-waveband catalog consisting of three WFC3 filters (F105W, F125W and F160W) and five ACS filters (F435W, F606W, F775W, F814W and F850LP). Any galaxy that was not detected in any of the above filters or which was not covered by imaging in any of the

filters was excluded from the catalog. The final data set consists of 20,512 objects out of an initial 34,930.

We use the spectral energy distribution (SED) fitting code LEPHARE (Arnouts et al. 1999; Ilbert et al. 2006), combined with the Bruzual & Charlot (2003) stellar population synthesis models, to derive the physical properties for each galaxy (stellar mass and star formation rate). We assume an exponentially declining star formation history with nine different e-folding times in the range of $0.01 < \tau < 30$ Gyr. The dust properties are modeled with varying $E(B - V)$ between 0 and 1.1 assuming the Calzetti et al. (2000) dust attenuation curve. We also take into account nebular emission line contribution as described in Ilbert et al. (2009) and assume a Chabrier initial mass function Chabrier (2003a), with lower and upper mass limits 0.01 Msun and 100 Msun respectively. We consider three different metallicity values: $Z = 0.02, 0.008, \text{ and } 0.004$.

LEPHARE produces a marginalized likelihood of stellar masses, and we use the median value of this likelihood as our stellar mass estimate. To measure the star formation rate (SFR), we use the rest-frame UV luminosity which traces timescales of ~ 100 Myr which is associated with continuum from massive, short-lived O and B type stars. We adopt the Salim et al. (2007) SFR(UV) calibration:

$$\log_{10} \text{SFR} = -0.4M_{\text{UV,AB}} - 7.53 \quad (1)$$

where $M_{\text{UV,AB}}$ is the dust-corrected monochromatic absolute UV magnitude in AB system. We measure the observed UV magnitude ($M_{\text{UV,observed}}$) by using the 1600Å flux density from the best-fit SED. The UV spectral slope (β_{UV}) is measured by fitting a power law of the form $f_{\lambda} \propto \lambda^{\beta_{\text{UV}}}$ between $1300\text{\AA} < \lambda < 2600\text{\AA}$ to the best-fit SED, with f_{λ} being the wavelength-dependent flux density. We dust correct the observed M_{UV} by assuming the Meurer et al. (1999) calibration:

$$M_{\text{UV}} = M_{\text{UV,observed}} - (1.99\beta_{\text{UV}} + 4.43) \quad (2)$$

where M_{UV} is the dust-corrected UV magnitude.

2.2. Semianalytic galaxies

We use mock catalogs generated from semianalytic models to mimic CANDELS observations, as presented in Lu et al. (2014). In short, a semianalytic model takes a cosmological dark-matter-only simulation and adds baryonic components with recipes for their evolution through cosmic time depending on the evolving properties of the dark matter host halo. This baryonic component can consist of stars, cold gas, hot gas, or a black hole, with various physical processes transferring

mass from one component into another (e.g., stars can form from cold gas).

The mock catalog we use was presented in Lu et al. (2014) as the ‘‘Lu’’ model. It assumes heating of the gas by reionization which, in turn, limits the fraction of the baryons that collapse into the halos (Gnedin 2000; Kravtsov et al. 2004). Radiative cooling is estimated assuming the Croton et al. (2006) model that collapses a fraction of the hot gas onto central (but not satellite) galaxies depending on the cooling timescale of the halo. As in other semianalytic models, the cold gas is assumed to be distributed in an exponential disk where stars are formed. A particular feature of model we use here is that the star formation rate depends on the circular velocity of the host halo in addition to the more typical dependences on star-forming gas mass and disk dynamical time scale. Supernova feedback reheats the cold gas and ejects both cold and hot gas. No explicit model for black hole accretion or AGN feedback is assumed, but a halo quenching model is implemented that switches off radiative cooling above a halo mass around $10^{12}M_{\odot}$. Galaxy mergers are handled by following subhalo information in the merger tree and assuming that even an unresolved subhalo will remain intact for some fraction of the dynamical friction time. A fraction of the mass in new stars is assumed to convert into metals and is instantly recycled back into the disk (and from there into the cold and hot gas surrounding the disk, according to the above prescriptions), parameterized using a Chabrier initial mass function (Chabrier 2003b).

The merger trees for our mock catalogs used were drawn from the Bolshoi N -body cosmological simulation (Klypin et al. 2011), with a volume of $(250 \text{ Mpc}/h)^3$, using 8 billion particles with a mass resolution of $1.35 \times 10^8 M_{\odot}$, and 180 stored time steps. Halo finding was performed with the Rockstar code (Behroozi et al. 2013a) and merger trees were constructed using the Consistent Trees algorithm (Behroozi et al. 2013b). Lightcone halo mock catalogs are extracted from the simulation box. These lightcone catalogs mimic the five CANDELS fields, and have redshift range from $z = 0$ to $z = 10$. Eight realizations are generated for each of the fields. Each dark matter halo in a lightcone catalog has a unique ID. The corresponding dark matter halo merger tree branch is found from the simulation box and rooted on the halo.

The model parameters used in Lu et al. (2014) are tuned to match calibration data. The main calibration set is the stellar mass function of local galaxies from Moustakas et al. (2013). Parameters were tuned using Markov Chain Monte Carlo chains with the differential evolution algorithm (Braak 2006) and a likelihood

based on a weighted χ^2 , with a parameterization to account for incompleteness in the data at low mass.

The best fit model is adopted to apply onto each merger tree of the lightcone mocks to predict the star formation history of each galaxy hosted by every halo in the mock. The semianalytic models contain simulated magnitudes for the eight CANDELS bands described above.

We only use galaxies from the mock catalog within the redshift range $0.1 < z < 6$. We also impose a cut such that the H -band AB magnitude is < 30 , to avoid a small population of high-mass low-magnitude galaxies that are separated in parameter space from the rest of the models, and are significantly fainter than them.

In the real world, the data contains observational uncertainties. To examine how much observational error degrades the best-case performance of our neural networks, we will also analyze the simulations with pseudo-“observational error” applied. We incorporate errors in the mock catalogs using the observational errors associated with CANDELS galaxies. We measure the median multiplicative flux error in bins of magnitude with width 0.5. These were then linearly interpolated to obtain a typical multiplicative uncertainty for a given magnitude in the data. We then draw a random Gaussian-distributed number δF with a scale length given by this multiplicative uncertainty, and add the term $\eta = -2.5 \log_{10}(1 + \delta F)$ to simulate observational errors. The simulation data perturbed in this way looks similar to the CANDELS data. This pseudo-observational error is added when the catalogs are read into our neural network software, before any colors are computed or any splitting into training and validation data sets is performed. We also explore a case where we mimic the noise properties of only well-resolved galaxies, defined as galaxies with flux signal-to-noise ratios ≥ 5 in each observed band. In both cases, after we have perturbed the magnitudes, we apply a cut to remove galaxies that have scattered below the minimum observed magnitude in each band.

2.3. Comparison of semianalytic models with CANDELS observations

The semianalytic models have been tuned to match observations (Lu et al. 2014). Here, we compare the galaxy magnitudes in both the noise-free and noisy case, to demonstrate the feasibility of using the semianalytic galaxies to train a neural network that is then applied to the CANDELS data.

In Fig. 1, we show color-color plots, with heatmaps showing the location of both the semianalytic galaxies (with and without simulated noise) and the observed

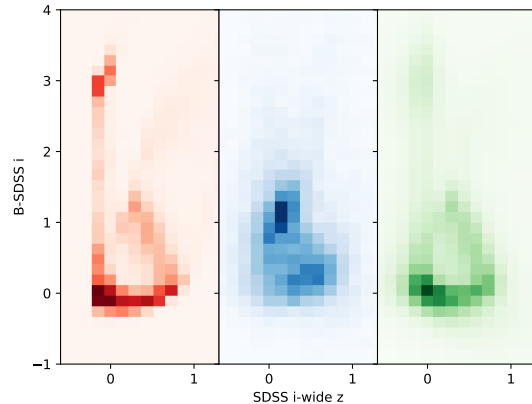


Figure 1. Color-color plots for one projection of the 8-dimensional color space. Left panel contains semianalytic galaxies without noise, center panel is CANDELS measurements, right panel is semianalytic galaxies with simulated photometric noise. The spanned color space is very similar; the vertical feature in the semianalytic plots missing from the CANDELS distribution consists of faint high-redshift galaxies below the CANDELS completeness limit.

CANDELS galaxies. We chose this projection of the higher-dimensional color space as good representatives of the general trend: the semianalytic galaxies without noise lie on thin manifolds, with the CANDELS galaxies being consistent with their overall trend but significantly broadened by observational noise, and the semianalytic galaxies with added noise looking similar to the CANDELS galaxies, but with some galaxies smeared outside the boundaries of the semianalytic and CANDELS galaxies by the noise. In the first panel, the vertical manifold at $i - z \approx -0.2$ in the semianalytic galaxies does not show up strongly in the data. However, this is expected, as the galaxies on that part of the manifold are at higher redshift and fainter, below the CANDELS completeness limit.

We do not expect our machine learning method to be affected by the presence of objects in our semianalytic sample that do not appear in the CANDELS data. It is more important that all CANDELS galaxies have good representation in the semianalytic data set. Having semianalytic objects outside the bounds of the CANDELS galaxies merely means that we have trained a machine learning method for data it will never see. The only exception would be if the faint semianalytic galaxies introduced a degeneracy in the color-space manifold that is not there for brighter galaxies. However, we do not see signs of this in our data set (the quality of the fit to brighter galaxies does not improve when excluding fainter galaxies).

3. MACHINE LEARNING PROCEDURE

Machine learning techniques have recently been adapted to problems in astronomy including photometric redshifts (e.g. Sánchez et al. 2014; Bilicki et al. 2017; Tanaka et al. 2018), large-scale structure (Aragon-Calvo 2018), galaxy morphologies (Domínguez Sánchez et al. 2018), and calibration factors for weak lensing data measurement algorithms (Tewes et al. 2018). In this work, we will be using the technique known as a neural network.

The idea of a neural network is simple. The underlying motivation is that we have a data vector (say galaxy colors), as well as a desired output (stellar mass, for example) that is a nonlinear function of that data vector, and we want to learn how to estimate the output given a new data vector. We don’t know the optimal form of the function, however, and even if we did, it is likely that the complicated form would make determining the parameter values difficult. Neural networks computationally determine the important combinations of the data points, and the appropriate coefficients for those combinations, by breaking the prediction process down into a series of linear combinations of the data points, combined with nonlinear transformations of those sums to reproduce nonlinear behavior.

As illustrated in Fig. 2 for a single data point, in the usual neural network setup, a set of vectors is fed to a layer of computational units called nodes. Each node computes a weighted sum of the coordinates of each vector, and optionally applies a simple nonlinear function to the sum (which might clip negative values, for example). The output of the layer—one value for each node for each input datapoint—can then act as a new set of vectors, which is fed to a new layer of nodes. The final layer has only one node, and the value it computes for each data point is the prediction, y_p , that corresponds to the true value of y for the data points. The free parameters of the model produced by the network are the weights used to compute the weighted sum in each node. To compute the optimal values of these parameters—a process called *training the network*—iterative adjustments are made based on a comparison of the predictions y_p to the known true values for the input data points y . The iterations proceed until either the desired accuracy is reached or the network stops improving its accuracy. A more detailed overview of this technique with additional complications can be found in Goodfellow et al. (2016). Error estimation can be performed by training multiple networks (e.g. Bilicki et al. 2017) but here we use a simple point estimate from a single network. In its simplest form, a neural network consists of a series of matrix multiplications with a simple function applied to

the outputs: for an input data point x with M features fed to a layer of N nodes, the output O_i of the i th layer is simply

$$O_i = f(W_i x + C_i) \quad (3)$$

where C_i is a scalar or vector of offsets and W_i is a matrix. The function $f(x)$ is chosen to fit the problem at hand, while the values of the matrices W_i are numerically trained to fit the training sample as described above. By convention, this function is called a “response function” in machine learning terminology. Again, the response function is usually nonlinear: if it is linear, then the whole network produces a simple linear combination of the input data. The computational difficulty of neural networks comes from the complexity of training the many values of the W matrices, and particularly the difficulty of training more than one or two layers (Goodfellow et al. 2016; Lanusse et al. 2018, and references therein). The initial values of W are typically set near 1 with small random offsets in each element (Abadi et al. 2015), meaning that (unless the random number generator is seeded in the exact same way) the same neural network architecture will produce slightly different predictions for the same training set.

The necessary choices to set up a neural network include:

- The number of layers
- The number of nodes in each layer
- The response functions f_i
- The method used to train the network (i.e., to alter the weight matrices W_i after each iteration)
- The function that computes a metric distance between the predicted points and the true values (called a *loss function*)

We use the Google package `TensorFlow`¹ (Abadi et al. 2015) to implement our neural network. `TensorFlow` is a highly-optimized framework designed to enable fast implementation of neural networks and other machine-learning problems. The package runs mostly compiled code to increase speed of execution, but the user interface is in Python. For this work, we use the high-level “Estimator” API for `TensorFlow`, which automates most of the bookkeeping necessary to setup and train a neural network. Our network has a set of 3 20-node layers; we found this architecture to be complex enough to reproduce high-dimensional nonlinear manifolds in color

¹ <https://www.tensorflow.org/>

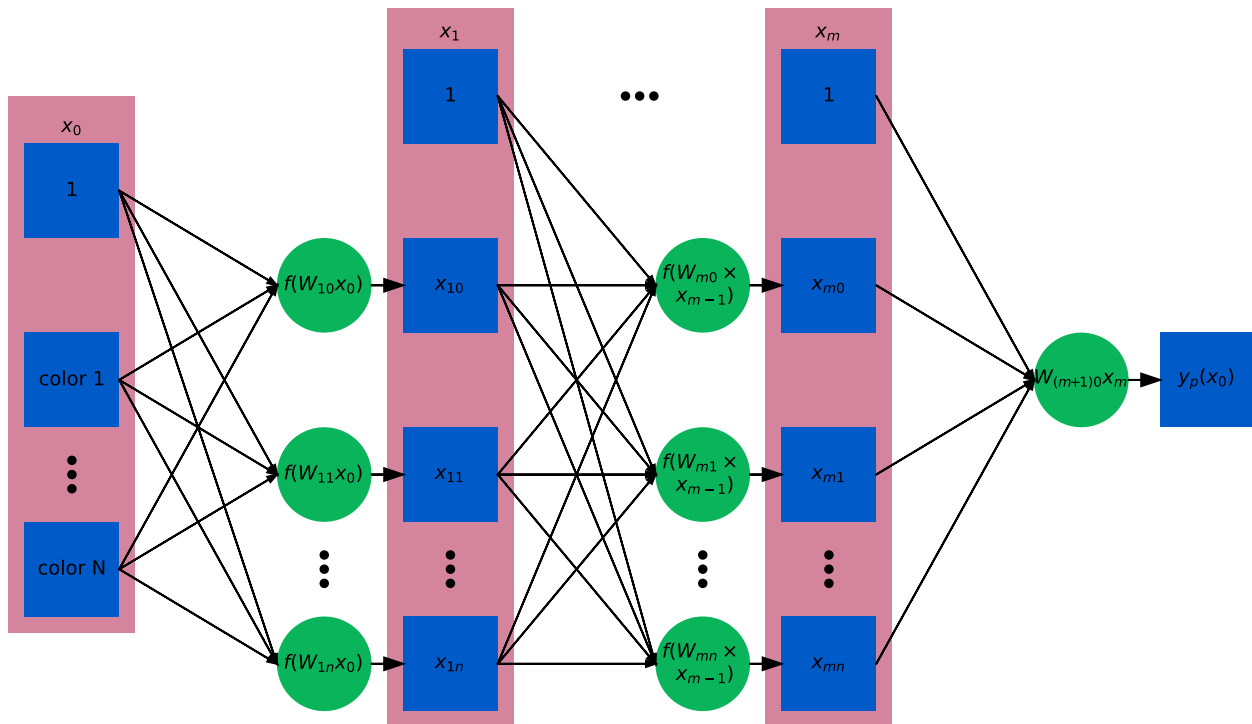


Figure 2. A schematic for a simple neural network. On the left, the inputs consist of N galaxy colors shown in blue boxes, plus a constant value to provide offsets. This vector of data (everything in the red rectangle labeled x_0) is passed to a layer of n nodes (the green circles); each node performs a weighted sum, and then performs a nonlinear transformation of the sum via $f(x)$. The outputs of this layer of nodes, along with another constant value, form a new vector, x_1 , which is itself fed to another layer of n nodes. This process repeats until we have fed the data through m layers. Finally, the outputs of the last layer, x_m , are fed to a single node that performs a weighted sum, and the value of this weighted sum is our prediction, y_p .

space, while still being simple enough that the neural network training algorithm could converge on a good solution. The response functions f_i in our network are the “relu”, or rectified linear unit, function (Glorot et al. 2011):

$$f(x) = \begin{cases} x & \text{if } x \geq 0, \\ 0 & \text{if } x < 0. \end{cases} \quad (4)$$

This satisfies the requirement that $f(x)$ is nonlinear in x to reproduce nonlinear behavior, while still being computationally efficient.

Our loss function is a simple squared distance between the labels y from our catalog and the predictions $y_p(x)$ from our neural network, summed over input training points k :

$$L = \sum_k (y_k - y_p(x_k))^2 \quad (5)$$

This is, of course, related to the χ^2 that is more commonly used. In this case, we do not normalize by the expected values y_k or expected uncertainty; we found that doing so has the effect of focusing the training first on small values of y_k , in practice making it more dif-

ficult to find a manifold that works well for the entire parameter range.

3.1. Training the network

To train the network, we split the data into two sets: a set to use to train the coefficients of the network, and a set to evaluate how well our network is reproducing the data. The two sets must be different in order to avoid overfitting, the problem where the network reproduces not only the average trends in the data, but the specific noise realization of the data set used for training (Goodfellow et al. 2016). We use a 70-30 split, with 70% of the data used to train the coefficients (called the “training set”) and 30% to check its performance at intervals (called the “validation set”).

We use stochastic gradient descent to train the network, in which we iteratively compute the predictions of the network on a random subset of our training data (Goodfellow et al. 2016). In our case, we find that using 10,000 points per step works well, with a check against the validation set every 500 steps ($5 \cdot 10^6$ total training data points passed through the network). We use

the Adam optimizer (Kingma & Ba 2014) to update the coefficients after every step. Briefly, the Adam algorithm involves an adaptive learning rate computed from moments of derivatives of the loss function, Eq. (5) so that the coefficients change more quickly when the gradient of the loss function is high, and then change only slowly as the loss function approaches a (local) minimum. We use the default parameter settings for the Adam optimizer implementation within TENSORFLOW. We explored changing the learning rate α , which controls how fast or slow the coefficients change for a given value of the loss function, but accuracy and precision decreased as we moved away from the default value.

4. APPLICATION TO SEMIANALYTIC GALAXIES

In our semianalytic catalog, each mock galaxy is associated with four physical parameters: stellar mass M_{star} , redshift z , stellar metallicity Z_{star} , and average star formation rate SFR .² There has been good progress in using machine learning techniques to measure photometric redshifts (Salvato et al. 2018). Therefore, we concentrate on measuring other parameters here.

We train networks using 5 possible sets of input data columns. We will use the bold letters in parentheses as shorthand in tables throughout the paper.

- Galaxy magnitudes (**m**)
- Galaxy pairwise colors ($B - V$, $V - i$, etc) (**c**)
- Galaxy magnitudes and pairwise colors (**mc**)
- All galaxy colors ($B - i$ in addition to $B - V$ and $V - i$, etc) (**C**)
- Galaxy magnitudes and all galaxy colors (**mC**)

Machine learning algorithms generally respond to information in different ways than the deterministic model-fitting methods more commonly used in astronomy. If the output is sensitive to a particular combination of data points (such as a color formed from two non-adjacent filters), then it is often more numerically efficient to give the algorithm this combination, even if the magnitudes are available to the algorithm to be subtracted internally. To some extent this is also dependent upon the training we are doing: we are, in some sense, optimizing the inputs for the architecture

² Other quantities in the catalog, for example the dark matter halo mass, will correlate with galaxy light properties because they correlate with, for example, the stellar mass; for this work, we consider only the direct correlations, not such indirect correlations, which pick up both additional parameters like the stellar-halo mass connection and additional noise.

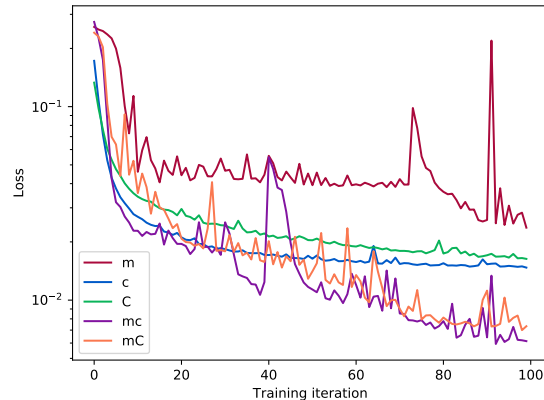


Figure 3. The loss function for the test set the first 100 training iterations (500 steps per iteration) in neural networks trained to reproduce stellar mass. Letter codes are different input column choices: m, magnitudes; c, pairwise colors; C, all colors. Training the network is a numerical optimization problem and does not always proceed monotonically.

of our network, in addition to optimizing the network that uses those inputs. A different set of layer and node parameters, or a different learning rate, for example, might respond differently to the choice of input values.

To quantify how well a networks performs, in addition to the loss function, we will report the mean bias, uncertainty, and 3σ outlier rate, computed for the parameter

$$b_k = y_k - y_p(x_k) \quad (6)$$

where, as above, y_k is the true value of the galaxy property for data point k , and $y_p(x_k)$ is the predicted value for the galaxy property computed using the vector x_k . We report $\langle b \rangle$, $\sigma_b = (\langle b^2 \rangle - \langle b \rangle^2)^{1/2}$, and the fraction of data points with $|(b_k - \langle b \rangle)/\sigma_b| > 3$.

In this section, we will train neural networks for each of the main galaxy properties, with these 5 different input column choices, and with and without simulated photometric noise. We then analyze the bias and uncertainties in the results.

4.1. Basic predictions

4.1.1. Stellar mass

Table 1 shows that we achieve the best performance when our input data includes galaxy magnitudes as well as the set of all colors (not just pairwise colors). The fact that using all colors optimizes the relation may be specific to our neural network setup: the non-pairwise colors can be computed from the pairwise colors, and another architecture might discover this relation.

Noise level	Input columns	Number of steps	Loss ^{1/2}	Average bias	Uncertainty	3 σ outlier rate
None	m	100000	0.157	-0.055	0.147	0.013
None	c	100000	0.115	0.003	0.115	0.016
None	C	100000	0.120	-0.021	0.119	0.018
None	mc	100000	0.071	-0.025	0.066	0.0147
None	mC	100000	0.058	-0.011	0.056	0.015
5 σ	mC	10000	0.124	0.007	0.124	0.012
Full noise	mC	10000	0.204	-0.019	0.203	0.018

Table 1. Summary of the performance of the neural networks for $\log_{10} M_{\text{star}}$. Input column codes are: m, magnitudes; c, pairwise colors; C, all colors. The best-performing metric for the noise-free case is highlighted in bold text. See section 4 for more details on column choices and performance metrics.

In Fig. 3, we show the value of the loss function as a function of the number of training steps for the different sets of input columns. The numerical nature of the algorithm is obvious from the non-monotonic behavior and sharp jumps in some of the lines. The magnitude-only or color-only networks, which did not perform as well for stellar mass, asymptote to relatively high values of the loss relatively early on; 100 steps in, however, the magnitude plus color networks are still improving.

In the absence of noise, our performance on $\log_{10} M_{\text{star}}$ is reasonable for individual galaxies, with overall biases a few percent or less and uncertainty of the order of 10 per cent, as shown in Table 1. The overall distribution is well reproduced by eye, and likely well reproduced enough for scientific applications, although distribution similarity tests such as the K-S test indicate that the distributions are statistically different. The error as a function of galaxy parameter in Fig. 4 demonstrates that we can train the networks well where there is a high density of points, but we have increased errors towards the tails of the distribution.

We now compare our results to stellar mass measurements of mock catalogs. Mobasher et al. (2015) performed a comprehensive study to estimate uncertainties and sources of bias in measuring physical parameters in galaxies. A number of different tests were performed, based on different initial parameters and codes. Here we adopt TEST-2A as our benchmark, as it is closest to our sample. TEST-2A used semianalytic models with a diversity of star formation histories and other parameters, and as with our semianalytic models, used measurements in CANDELS filter bands as their data set. We note that TEST-2A used more CANDELS bands than our measurement here: 13 instead of 8, including U-band, K-band, and Spitzer infrared data in addition to the Hubble optical and near-infrared bands we use, and excluding the F184W (ACS) filter that we use. Comparing to the distribution of biases and uncertain-

ties returned by the individual methods in Mobasher et al. 2015, we find that we easily improve on the bias and have competitive uncertainty in our measurements. However, we expect to have lower bias: different assumptions of initial mass functions, star formation rates, etc were found by Mobasher et al. 2015 to be a source of systematic offsets between different codes, adding a constant bias to every galaxy, whereas we are implicitly assuming the same initial mass function and star formation rate since our samples are drawn from the same mock catalog. Our templates also have varying amounts of dust and varying metallicities, the lack of which has also been found to bias stellar mass estimates (Mitchell et al. 2013).

We repeat the analysis with pseudo observational error, either matched to the full uncertainty distribution or matched to the uncertainty distribution of galaxies which have at least a 5 σ -detected flux measurement in each band. We show only the best-performing input column set from the noise-free case, after checking that this column choice still performs best when error is added. This additional simulated observational noise causes an increase in bias and a large increase in uncertainty, visible in the right-hand plots of Fig. 4. However, the average bias of -0.019 dex is still smaller by an order of magnitude than any of the biases from Mobasher et al. (2015) (with the same caveat about correct implicit assumptions), and the uncertainty only a little worse than the maximum uncertainty from that comparison, 0.203 dex instead of 0.183 dex.

4.1.2. Metallicity

As with stellar mass, we find good performance from our metallicity-predicting neural networks, with small biases and order 10 per cent uncertainty, as shown in Table 2 and Fig. 5. The overall predicted distribution is somewhat more skewed from the original distribution than in the stellar mass case, though again we perform well where the density of training points is high. As with

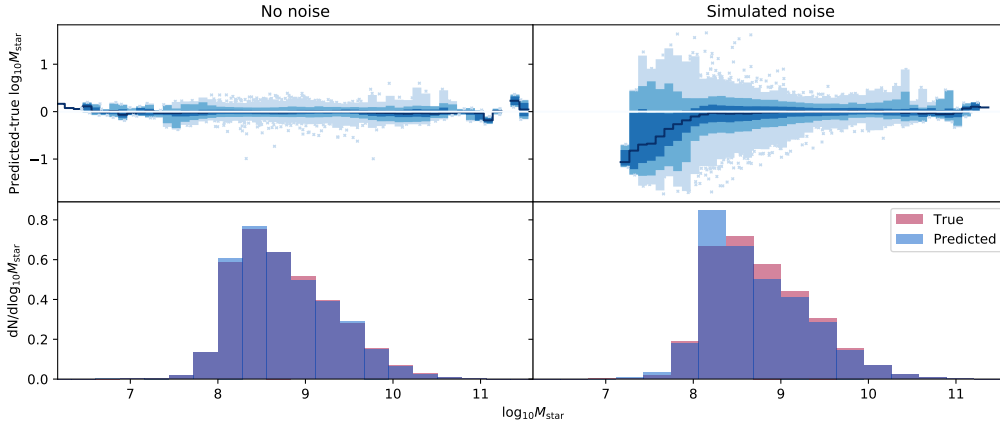


Figure 4. Neural network performance reproducing stellar mass on the validation set of the simulation galaxies. Left panels are noise-free, right panels have simulated observational noise. Top panels: Prediction error relative to the true values as a function of predicted stellar mass. Performance is shown in bins of size $\Delta \log_{10} M_{\text{star}} = 0.1$, and the median and 1-, 2-, and 3σ percentile contours are shown as the dark blue line and the three lighter blue regions, respectively. Outliers are shown as light-blue crosses. The white line is zero bias. The bias is low in the intermediate range of stellar masses, where most of the training points are, but increases at low and high stellar mass. Bottom panel: The histograms of predicted and actual stellar mass, which are similar in shape for the noise-free case, though the predicted stellar mass peaks at a slightly lower value than the truth. The predicted distribution is significantly skewed in the noisy case relative to the expected distribution.

Noise level	Input columns	Number of steps	Average Loss ^{1/2}	Average bias	3 σ outlier Uncertainty	3 σ outlier rate
None	m	100000	0.092	0.002	0.092	0.013
None	c	100000	0.075	0.010	0.074	0.015
None	C	100000	0.064	-0.001	0.064	0.017
None	mc	100000	0.070	0.007	0.069	0.014
None	mC	100000	0.065	0.017	0.062	0.0137
5 σ	C	10000	0.149	-0.008	0.149	0.011
Full noise	C	10000	0.204	-0.035	0.201	0.015

Table 2. Summary of the performance of the neural networks for $\log_{10} Z_{\text{star}}$. Input column codes are: m, magnitudes; c, pairwise colors; C, all colors. The best-performing metric for the noise-free case is highlighted in bold text. See section 4 for more details on column choices and performance metrics.

stellar mass, we perform worse when noise is included, but not by a significant amount: an increase of bias by a factor of 2 and uncertainty by a factor of 3. This uncertainty, of 0.2 dex in the full-noise case, is larger than the convolutional neural network machinery of Wu & Boada (2018), who obtained 0.08 dex uncertainty, albeit using substantially more data (3-color 128x128 pixel cutouts, not eight measured magnitudes) and brighter and lower-redshift galaxies (brighter than 25th magnitude). We obtain a similar result to theirs in that low-metallicity galaxies have systematically high metallicity predictions in the presence of noise.

This good performance on metallicity requires some discussion. Metallicity is typically the hardest of these properties to measure by traditional methods so it is

surprising that we are able to do well. The dominant component of our performance is driven by the relationship between metallicity and stellar mass. There is a strong relationship between these quantities in data and in simulation (Lu et al. 2014, and references therein), and in practice the fact that we can fit stellar mass well means that most of our prediction of metallicity comes from the ability of the network to learn the $M_{\text{star}} - Z_{\text{star}}$ connection and to predict M_{star} from the photometry, as can be seen by the similar shape of the bias-parameter curves in the noisy right-hand columns of in Fig. 4 and Fig. 5. That cannot be the full picture—metallicity performs best when we use colors alone, while stellar mass performs best when we use both magnitudes and colors—but it is a significant contributor to our good results.

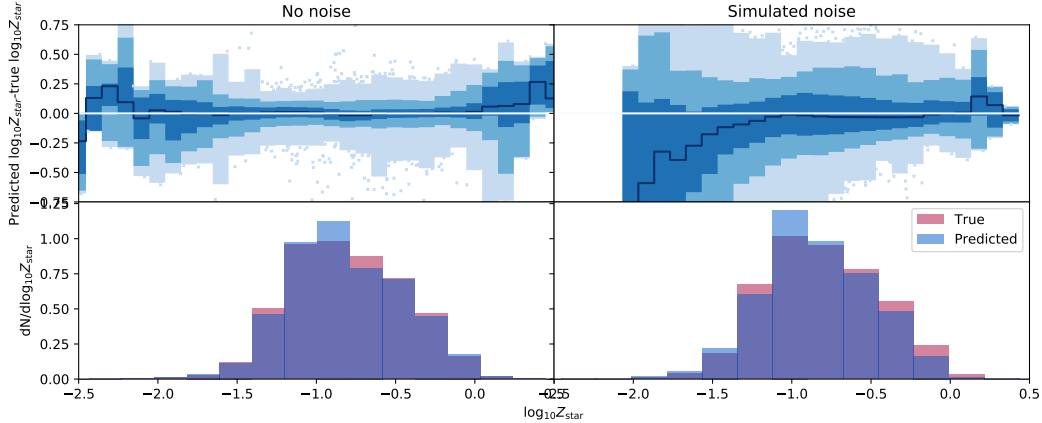


Figure 5. Neural network performance reproducing stellar metallicity on the validation set of the simulation galaxies. Left panels are noise-free, right panels have simulated observational noise. Top panel: Prediction error relative to the true values as a function of predicted stellar metallicity. Performance is shown in bins of size $\Delta \log_{10} Z_{\text{star}} = 0.1$, and the median and 1-, 2-, and 3σ percentile contours are shown as the dark blue line and the three lighter blue regions, respectively. Outliers are shown as light-blue crosses. The white line is zero bias. As with stellar mass, we perform well for metallicities in the middle of the metallicity range where the density of training points is high, but we see increased bias and, here, increased uncertainty for points with low or high metallicity. Bottom panel: The histograms of predicted and actual stellar metallicity. Here, it is clear that the predicted metallicities have a narrower distribution than the true metallicities even in the noise-free case.

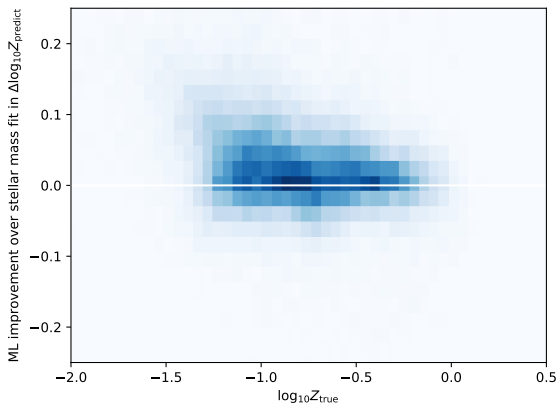


Figure 6. A 2-D distribution showing the improvement in metallicity estimation made by our neural network, relative to a simple model that uses the mean $M_{\text{star}} - Z_{\text{star}}$ relation. Points above the white line at 0 have a neural network prediction that is closer to the true value of Z_{star} than the simple model prediction. The bulk of the points are above 0, indicating that the neural network is improving on the simple model, but the amplitude of the improvement indicates that the bulk of the correlation is being driven by the $M_{\text{star}} - Z_{\text{star}}$ relation and not an independent measurement of metallicity.

To illustrate this, we fit a simple quadratic equation to the $\log_{10} M_{\text{star}} - \log_{10} Z_{\text{star}}$ relationship in the simulations to predict a metallicity for each galaxy assuming no noise, and then we check how much improvement we get from the noise-free neural network when compared

to this simple M_{star} -based prediction. Fig. 6 shows a 2-D histogram of this improvement, with points above 0 being an improvement on the polynomial fit, and points below 0 having an increased bias. The bulk of our neural network predictions do improve on the simple model, by $1-2\sigma$, but given that our data spans more than 2 orders of magnitude, an improvement of 0.1-0.2 dex indicates that the simple stellar mass-metallicity relationship can explain a good fraction of our predicted metallicities. The additional improvement is also suggested by the fact that the metallicity network performs better without magnitudes, while the stellar mass network performs better with them, meaning that the metallicity network must be learning different information than stellar mass alone. Still, this effect suggests that, for any method, if metallicity is not well-constrained by the data, using a stellar mass-based prior with appropriate uncertainty may produce adequate results.

4.1.3. Star formation rate

For the star formation rate, we have slightly higher bias and uncertainty. The bias of -0.053 dex corresponds to a 12 percent error in linear space, visible in the histogram of Fig. 7 as the blue prediction histogram peaking slightly higher than the true distribution in red. Much of the uncertainty is contributed by points with very low star formation rates. Fig. 7 shows the performance as a function of predicted star formation rate as well as a histogram of true and predicted values.

4.2. Redshift effects

Noise level	Input columns	Number of steps	Loss ^{1/2}	Average bias	Uncertainty	3 σ outlier rate
None	m	100000	0.297	-0.063	0.291	0.016
None	c	100000	0.178	-0.014	0.178	0.015
None	C	100000	0.179	-0.004	0.179	0.016
None	mc	100000	0.142	0.019	0.141	0.014
None	mC	100000	0.150	0.053	0.141	0.012
5 σ	mC	10000	0.213	-0.043	0.227	0.018
Full noise	mC	10000	0.296	-0.088	0.304	0.023

Table 3. Summary of the performance of the neural networks for $\log_{10} SFR$. Input column codes are: m, magnitudes; c, pairwise colors; C, all colors. The best-performing metric for the noise-free case is highlighted in bold text. See section 4 for more details on column choices and performance metrics.

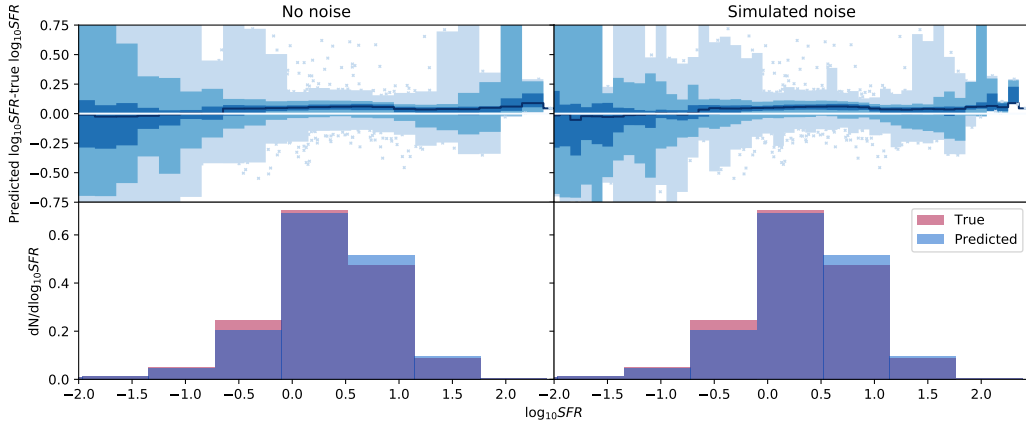


Figure 7. Neural network performance reproducing average star formation rate on the validation set of the simulation galaxies. Left panels are noise-free, right panels have simulated observational noise. Top panel: Prediction error relative to the true values as a function of predicted average star formation rate. As in the above figures, the median and 1-, 2-, and 3 σ percentile contours are shown as the dark blue line and the three lighter blue regions, respectively. Outliers are shown as light-blue crosses. The white line is zero bias. The large uncertainty in average star formation rate can be seen clearly, with an order of magnitude in uncertainty for the least star-forming galaxies. A bias is visible even in the well-constrained regions near the peak of the star formation rate distribution. Bottom panel: The histograms of predicted and actual star formation rate. The histograms are not markedly different, although the difference is significant given the number of objects in each bin..

Property	Input columns	Number of steps	Loss ^{1/2}	Average bias	Uncertainty	Δ bias	Δ uncertainty
M_{star}	mCz	100000	0.046	-0.010	0.045	0.001	0.011
Z_{star}	Cz	100000	0.078	0.009	0.077	-0.008	-0.013
SFR	mCz	100000	0.136	-0.004	0.136	-0.049	0.005

Table 4. Summary of the performance of the neural network for different predictions when redshift is included as an input column. Input column codes are as in Table 3. We show only the best-performing input column set from the case without using redshifts to examine the improvement redshift provides. See section 4 for more details on column choices and performance metrics. We note that the value of bias for star formation rate, -0.004, is a chance noise fluctuation down relative to the performance of the network, and the bias for a different subset of the data would likely be larger.

None of these networks used redshift as an input, but template-fitting methods generally require it (Mobasher et al. 2015). Do our results improve if we add redshift as an input to the networks trained on the other galaxy properties? We take the best-performing input column set for stellar mass, metallicity, and star formation rate, and add redshift as an input. The results are summarized in Table 4. For stellar mass and star formation rate, the mean bias and the uncertainty both improve. However, the improvement in the uncertainty is generally small, and the change in bias is less than the uncertainty for all three galaxy properties. This is an encouraging result, as it means we can achieve good accuracy without needing to supplement our data with spectroscopic redshifts.

5. PERFORMANCE ON CANDELS DATA

We need to explore if networks trained on semianalytic models can be applied to observed galaxy data. We use the CANDELS data from the GOODS-S field described in Section 2.1, with the physical parameters measured through template fitting. From Mobasher et al. (2015), we know that different template-fitting methods can result in differences in the stellar masses of 0.2 dex. This gives an estimate of the accuracy we should aim for in our estimate of the stellar mass by this neural network technique.

We show the performance of the networks for all three noise cases (no noise, noise similar to galaxies with $> 5\sigma$ detections, and noise similar to the full CANDELS data set) in Table 5. The neural networks trained on semianalytic data without observational noise do not reproduce the data well. This is not surprising: the power of neural networks is that they reproduce high-dimensional nonlinear structure, so perturbing the data by some error has nonlinear effects on the prediction. As we add noise, the performance on the data improves, even though the performance on the mock catalogs worsens. Interestingly, we sometimes obtain lower bias or uncertainty when the method is applied to CANDELS data than we did on the simulations. This is because the simulations contain a larger population of faint galaxies than the CANDELS data, and the increased relative noise in fainter galaxies decreases the accuracy and precision of our predictions. We show the performance of the full noise case for two quantities (M_{star} and SFR , as the template-fitting outputs did not include metallicity) in Fig. 8. The fact that the networks perform better for noisier data indicates that some subtle difference between the simulation and the real galaxies is a likely culprit for some of our bias and uncertainty in the real data. Adding simulated noise, as we have done here, is

not a perfect solution, since selection cuts to match the CANDELS data were applied to the noise-free data.

The difference between the neural network predictions and the template-fitting predictions for the stellar mass are within our expectation of 0.2 dex for differences between template-fitting methods with different assumptions. However, the star formation rate numbers are significantly more discrepant, although even that difference is likely explained by a combination of different assumptions and differences in the data, rather than by differences in the data alone. The large uncertainty in both measurements is likely also due to a combination of different template-fitting assumptions and different data; we cannot tell which effect is dominant from our measurements alone.

6. SUMMARY AND DISCUSSION

We train neural networks on semianalytic models to predict from photometric data three galaxy properties of scientific interest: stellar mass, stellar metallicity, and average star formation rate. In the absence of noise—the best-case scenario—we achieve excellent accuracy and precision on all properties, indicating that the mapping between galaxy properties and galaxy photometry has low enough noise and few enough degeneracies to be a good target for neural networks. Injecting artificial photometric noise degrades the performance on a reserved sample of semianalytic galaxies, but allows the algorithm to perform better on real data from CANDELS, which contains noise.

Our accuracy and precision show that semianalytic galaxies can be used to train neural networks that can produce photometric stellar masses, metallicities, and star formation rates, and that these galaxy properties are accessible targets for machine learning. However, our performance on noisy simulated data is not yet fully competitive with mature template-fitting and machine-learning methods from the literature. There are several likely reasons for this discrepancy. First, many of these methods have been under development for years and have reached a level of complexity not matched by our simple implementation here. Second, because our model includes many more free parameters, we may be trading off precision (a narrower set of outputs generated by a template) with accuracy: our mean bias is lower for stellar mass, as we mentioned above, but our uncertainty is higher. Third, as mentioned in Section 4.1.2, we have used a wide range of fluxes and redshifts, a calibration set that may be more ambitious than some of the data sets we are comparing to. Still, as a first-step implementation of neural networks on this data, we have achieved good accuracy in predicting all galaxy properties.

Property	Input columns	Number of steps	Noise property	Average bias	Average Uncertainty	3σ outlier rate
M_{star}	mC	10000	No noise	0.270	0.950	0.014
M_{star}	mC	10000	5σ cut	0.208	0.581	0.029
M_{star}	mC	10000	Full noise	0.149	0.559	0.023
SFR	mC	10000	No noise	-1.06	2.14	0.019
SFR	mC	10000	5σ cut	-0.591	1.43	0.029
SFR	mC	10000	Full noise	-0.605	1.37	0.031

Table 5. Summary of the performance of the neural network trained on semianalytic galaxies with simulated photometric noise and applied to CANDELS data for different predictions. Input column codes are as in Table 3.

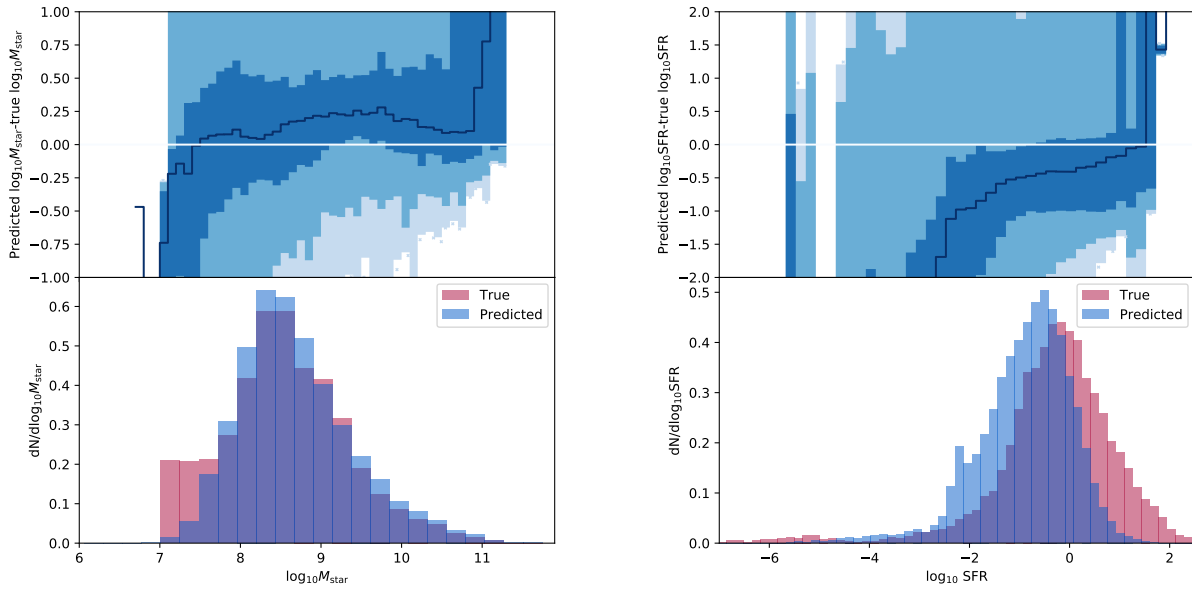


Figure 8. Summary statistics of performance of the neural network trained on semianalytic galaxies with simulated photometric noise and applied to CANDELS data. In each subfigure, the top panel shows the prediction error relative to the true values as a function of the predicted value for the galaxy property, and the bottom panel shows a histogram of the distributions of the galaxy property in the data and in our predictions. As before, in the top panel, the blue bars are the 1-, 2-, and 3σ percentile contours, while the median is in dark blue and the white line is zero error. The left-hand pair is stellar mass, and the right-hand pair is average star formation rate. Because the distributions are not symmetric about the median, the median biases shown in this figure are not equal to the mean bias from Table 5.

The performance on real CANDELS data is not as accurate or precise as comparison data sets from the literature (Mobasher et al. 2015). Some of that is driven by our decreased accuracy in the presence of noise even for the semianalytic galaxies, although the fact that the galaxies in CANDELS are brighter, on average, than our semianalytic galaxies means that in some cases we do better on the average CANDELS galaxy than we do on the average semianalytic galaxy. Also, we note that the photometry in the semianalytic catalog was de-

signed to match the CANDELS observed distributions, but since the CANDELS data are noisy and the semianalytic galaxies are not, we expect some mismatch between the locations of the underlying noise-free manifolds. Additionally, we do not expect perfect agreement, since the template-fitting results rely on other parameters (such as redshift and metallicity) that may differ from the values in our semianalytic catalogue; these differences in assumptions explain some of our observed discrepancies.

Interestingly, our results show that adding redshift information to our training sample results in either minor improvement or in degradation of accuracy and precision, indicating that the networks are capable of learning the relevant mapping between color, redshift, and other galaxy properties without explicit redshift information. This indicates that competitive accuracy and precision can be achieved even for galaxies that lack spectroscopic redshifts, greatly increasing the available sample sizes for future studies.

We are able to obtain good accuracy and precision for stellar metallicities, which is traditionally the most difficult to measure of the galaxy properties. This accuracy and precision is driven by a strong relationship between metallicity and stellar mass. We improve on the accuracy obtained by simply relying on a stellar mass–metallicity relation, but the improvement is order 0.1 dex, compared to the more than two orders of magnitude range in the parameter space, indicating that the predictive accuracy is dominated by the stellar mass–metallicity relation. This suggests the use of a strong stellar mass–metallicity prior when trying to obtain stellar metallicities from low-resolution data.

Future work will be needed to develop the machine learning architecture to a higher level of complexity and precision in order to be competitive in accuracy with currently-existing methods. However, our work shows that simple machine learning methods that do not know about the physics of galaxy formation and evolution can in principle reproduce galaxy property measurements

with high accuracy, as long as the training set and the data of interest are consistent with one another and the machine learning is carefully trained to handle degeneracies and noise in the data. This allows for not only the use of semianalytic models as a training set for galaxy property measurement, but also a multiplication of template-fitting efforts—for example, if template-fitted stellar masses are available for a representative spectroscopic subset of a large photometric survey, then machine learning is a computationally efficient way to extend those template-fitting results to the larger photometric data set. As we have shown here, machine learning methods can learn even complicated relationships between galaxy properties and photometry measurements drawn from a small number of filters, indicating that scientifically interesting galaxy properties can be measured with reasonable computational time on future datasets from large-scale photometric surveys.

Support for this work was provided by the University of California Riverside Office of Research and Economic Development through the FIELDS NASA-MIRO program. A portion of this research was carried out at the Jet Propulsion Laboratory, California Institute of Technology, under a contract with the National Aeronautics and Space Administration. We would like to acknowledge Dritan Kodra for the updated CANDELS photometric redshift catalog.

REFERENCES

- Abadi M., et al., 2015, TensorFlow: Large-Scale Machine Learning on Heterogeneous Systems, <https://www.tensorflow.org/>
- Abdalla F. B., Banerji M., Lahav O., Rashkov V., 2011, *MNRAS*, **417**, 1891
- Aragon-Calvo M. A., 2018, preprint, ([arXiv:1804.00816](https://arxiv.org/abs/1804.00816))
- Arnouts S., Cristiani S., Moscardini L., Matarrese S., Lucchin F., Fontana A., Giallongo E., 1999, *MNRAS*, **310**, 540
- Ball N. M., Brunner R. J., Myers A. D., Strand N. E., Alberts S. L., Tchong D., 2008, *ApJ*, **683**, 12
- Behroozi P. S., Wechsler R. H., Wu H.-Y., 2013a, *ApJ*, **762**, 109
- Behroozi P. S., Wechsler R. H., Wu H.-Y., Busha M. T., Klypin A. A., Primack J. R., 2013b, *ApJ*, **763**, 18
- Bilicki M., et al., 2017, preprint, ([arXiv:1709.04205](https://arxiv.org/abs/1709.04205))
- Bolzonella M., Miralles J.-M., Pelló R., 2000, *A&A*, **363**, 476
- Bouwens R. J., et al., 2010, *ApJL*, **709**, L133
- Braak C. J. F. T., 2006, *Statistics and Computing*, **16**, 239
- Brammer G. B., van Dokkum P. G., Coppi P., 2008, *ApJ*, **686**, 1503
- Bruzual G., Charlot S., 2003, *MNRAS*, **344**, 1000
- Calzetti D., Armus L., Bohlin R. C., Kinney A. L., Koornneef J., Storchi-Bergmann T., 2000, *ApJ*, **533**, 682
- Carrasco Kind M., Brunner R. J., 2013, *MNRAS*, **432**, 1483
- Carrasco Kind M., Brunner R. J., 2014, *MNRAS*, **442**, 3380
- Chabrier G., 2003a, *PASP*, **115**, 763
- Chabrier G., 2003b, *PASP*, **115**, 763
- Croton D. J., et al., 2006, *MNRAS*, **365**, 11
- Dahlen T., et al., 2013, *ApJ*, **775**, 93
- Dawson K. S., et al., 2013, *AJ*, **145**, 10
- Domínguez Sánchez H., Huertas-Company M., Bernardi M., Tuccillo D., Fischer J. L., 2018, *MNRAS*, **476**, 3661
- Drinkwater M. J., et al., 2010, *MNRAS*, **401**, 1429
- Driver S. P., et al., 2012, *MNRAS*, **427**, 3244

- Drlica-Wagner A., et al., 2018, *ApJS*, **235**, 33
- Freeman P. E., Newman J. A., Lee A. B., Richards J. W., Schafer C. M., 2009, *MNRAS*, **398**, 2012
- Gerdes D. W., Sypniewski A. J., McKay T. A., Hao J., Weis M. R., Wechsler R. H., Busha M. T., 2010, *ApJ*, **715**, 823
- Giavalisco M., et al., 2004, *ApJL*, **600**, L93
- Glorot X., Bordes A., Bengio Y., 2011, in Gordon G., Dunson D., Dudk M., eds, Proceedings of Machine Learning Research Vol. 15, Proceedings of the Fourteenth International Conference on Artificial Intelligence and Statistics. PMLR, Fort Lauderdale, FL, USA, pp 315–323, <http://proceedings.mlr.press/v15/glorot11a.html>
- Gnedin N. Y., 2000, *ApJ*, **542**, 535
- Goodfellow I., Bengio Y., Courville A., 2016, Deep Learning. MIT Press
- Grogin N. A., et al., 2011, *ApJS*, **197**, 35
- Guo Y., et al., 2013, *ApJS*, **207**, 24
- Hildebrandt H., et al., 2010, *A&A*, **523**, A31
- Hogan R., Fairbairn M., Seeburn N., 2015, *MNRAS*, **449**, 2040
- Ilbert O., et al., 2006, *A&A*, **457**, 841
- Ilbert O., et al., 2009, *ApJ*, **690**, 1236
- Kingma D. P., Ba J., 2014, CoRR, abs/1412.6980
- Klypin A. A., Trujillo-Gomez S., Primack J., 2011, *ApJ*, **740**, 102
- Koekemoer A. M., et al., 2011, *ApJS*, **197**, 36
- Kravtsov A. V., Gnedin O. Y., Klypin A. A., 2004, *ApJ*, **609**, 482
- LSST Science Collaboration et al., 2009, preprint, ([arXiv:0912.0201](https://arxiv.org/abs/0912.0201))
- Lanusse F., Ma Q., Li N., Collett T. E., Li C.-L., Ravanbakhsh S., Mandelbaum R., Póczos B., 2018, *MNRAS*, **473**, 3895
- Laureijs R., et al., 2011, preprint, ([arXiv:1110.3193](https://arxiv.org/abs/1110.3193))
- Lilly S. J., et al., 2007, *ApJS*, **172**, 70
- Lima M., Cunha C. E., Oyaizu H., Frieman J., Lin H., Sheldon E. S., 2008, *MNRAS*, **390**, 118
- Lu Y., et al., 2014, *ApJ*, **795**, 123
- Masters D., et al., 2015, *ApJ*, **813**, 53
- Meurer G. R., Heckman T. M., Calzetti D., 1999, *ApJ*, **521**, 64
- Mitchell P. D., Lacey C. G., Baugh C. M., Cole S., 2013, *MNRAS*, **435**, 87
- Mobasher B., et al., 2015, *ApJ*, **808**, 101
- Moustakas J., et al., 2013, *ApJ*, **767**, 50
- Riess A. G., et al., 2007, *ApJ*, **659**, 98
- Sadeh I., Abdalla F. B., Lahav O., 2016, *PASP*, **128**, 104502
- Salim S., et al., 2007, *ApJS*, **173**, 267
- Salvato M., Ilbert O., Hoyle B., 2018, *Nature Astronomy*,
- Sánchez C., et al., 2014, *MNRAS*, **445**, 1482
- Spergel D., et al., 2015, preprint, ([arXiv:1503.03757](https://arxiv.org/abs/1503.03757))
- Tanaka M., et al., 2018, *PASJ*, **70**, S9
- Tewes M., Kuntzer T., Nakajima R., Courbin F., Hildebrandt H., Schrabback T., 2018, preprint, ([arXiv:1807.02120](https://arxiv.org/abs/1807.02120))
- Windhorst R. A., et al., 2011, *ApJS*, **193**, 27
- Wu J. F., Boada S., 2018, preprint, ([arXiv:1810.12913](https://arxiv.org/abs/1810.12913))